Theoretical and Experimental Investigation of Voltage Current Characteristic, Losses and Self-discharge of a Vanadium Redox Flow Battery System

Richard Beyer(✉) and Thilo Bocklisch

Chair of Energy Storage Systems, Technische Universität Dresden, Dresden, Germany
richard_beyer@tu-dresden.de

Abstract. The paper describes results of the theoretical and experimental investigation and the modeling of a 5 kW and 15 kWh vanadium redox flow battery system (VRFBS). The first part of the paper presents the dependence of the voltage-current characteristics on state of charge (SOC), temperature, and electrolyte flow rate, as well as models for the stack overvoltages based on current literature. Furthermore, losses due to shunt currents, vanadium diffusion and power consumption of peripheral equipment are discussed. The second part of the paper presents new results of experimental investigations and the modeling of the self-discharge behavior of the VRFBS during the standby phase (open circuit operation, when no electric and electrolyte currents present) and the phase directly after restart of the VRFBS.

Keywords: Vanadium Redox Flow Battery System (VRFBS) · voltage current characteristic · self-discharge · shunt current · vanadium diffusion · energy storage · modeling

1 Introduction

Electrical energy storage systems are necessary for the efficient integration and utilization of renewable energy sources and for the balancing of occurring power fluctuations in the energy system. Vanadium redox flow battery systems (VRFBS) prove to be a very promising and sustainable energy storage technology due to their independent scalability of capacity and power as well as their good operating characteristics and recyclability [1].

This paper describes results of the theoretical and experimental investigations and the modeling of a 5 kW and 15 kWh VRFBS. The dependence of the voltage current characteristics on state of charge (*SOC*), temperature, and electrolyte flow rate are examined. Models for the stack overvoltages as well as losses due to shunt currents, vanadium diffusion and power consumption of peripheral equipment are discussed based on actual literature. Moreover, new insights of the self-discharge behavior of VRFBS for the standby phase (no electric and electrolyte currents applied to the system) are presented as results of experimental investigations.

P. Schossig et al. (Eds.): IRES 2022, AHE 16, pp. 47–62, 2023.
https://doi.org/10.2991/978-94-6463-156-2_5

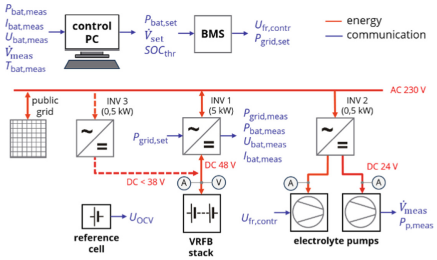

Fig. 1. Structure and subcomponents of the reference vanadium redox flow battery system.

The paper is structured as follows, Sect. 2 describes the reference plant. Section 3 describes the main modeling approaches for the cell behavior and the other system components and derives corresponding models for the electrical, electrochemical and fluid mechanical relationships. Section 4 shows the results of experimental investigations on the losses due to self-discharge processes in the VRFBS, especially during and after the standby phase. Finally, Sect. 5 summarizes the main results of the work and gives a brief outlook on follow-up work.

2 System Design

Figure 1 shows the basic structure and main components of the studied VRFBS, which was developed for use in grid-connected stationary industrial applications [2]. The VRFBS consists of a battery stack with 40 cells and a net power of 5 kW, a reference cell for monitoring purpose, the electrolyte pumps, the electrolyte reservoirs with an equivalent energy content of 15 kWh, the stack inverter, the power converters for auxiliary power supply, and a battery management system (BMS). The power of the VRFBS is adjusted via bidirectional inverter (INV 1) by controlling the stack voltage. Additional power converters are installed to supply the electrolyte pumps (INV 2) and to function as an auxiliary power unit (INV 3). The central control, safety and monitoring tasks are performed by the battery management system. This includes the control of the electrolyte flow rate as a function of the stack current. The specification of the most important operating parameters and the setpoint values as well as the storage of all operating data is carried out via a measuring and control computer and the higher-level energy management system.

3 Modeling Approach

3.1 Basics

The model approaches, for the concentration changes in the cells $dc_{c,i}$ and the reservoirs $dc_{r,i}$, the SOC, the open circuit voltage (OCV) U_{OCV}, the ohmic overvoltages U_{ohm}, the concentration overvoltages U_{cop}, and the concentration change due to vanadium diffusion $\Delta c_{c,i,dif}$ are derived according to the current state of the art based on [3–5]. Equivalent circuit models were used to calculate the electrical behavior as well as

the shunt currents. The loss and terminal behavior of the pumps and converters was described using lookup tables. The most important model blocks and their links are shown in Fig. 2. Model input variables are the required power of the VRFBS and the voltage of the VRFBS in the previous time step. The overall model was implemented in an object-oriented manner under MATLAB and Simulink with a variable simulation time step size of ≥1 s. Extensive experimental investigations were carried out to study the system behavior and determine model parameters. For this purpose, the VRFBS was set up in an air-conditioned room with a constant ambient temperature of $T_{amb} = 298.15\ K$. The modeling of thermal processes was not the subject of this work.

3.1.1 Electrolyte Concentration in Cells and Reservoirs

In the following, the oxidation states of the vanadium are described with the indices *(2,3,4,5)*. In a simplified way VO^{2+} is designated V^{4+} and $VO_2{}^{+}$ is designated V^{5+}. In general, the concentration c in $molm^{-3}$ of a vanadium species i is given by the ratio of the amount of substance n_i to the total volume V according to Eq. (1).

$$c_i = \frac{n_i}{V} \tag{1}$$

For the present work, it is necessary to distinguish different areas of the VRFBS with different concentrations. The total vanadium concentration c_v in the system is given as *1600* mol/m3. First, the positive and negative electrolyte circuits are considered separately, with the concentrations c_2/c_3 and c_4/c_5, respectively. A further subdivision of the concentrations in the subsections of the electrolyte circuits is made into the areas reservoir $c_{r,i}$ or cell inlet $c_{c,i,in}$ and cell outlet $c_{c,i,out}$ (s. Figure 3), since significant concentration changes occur at these points due to the cell reactions. In addition, an average cell concentration $c_{c,i,m}$ is formed as the mean value of the concentration in

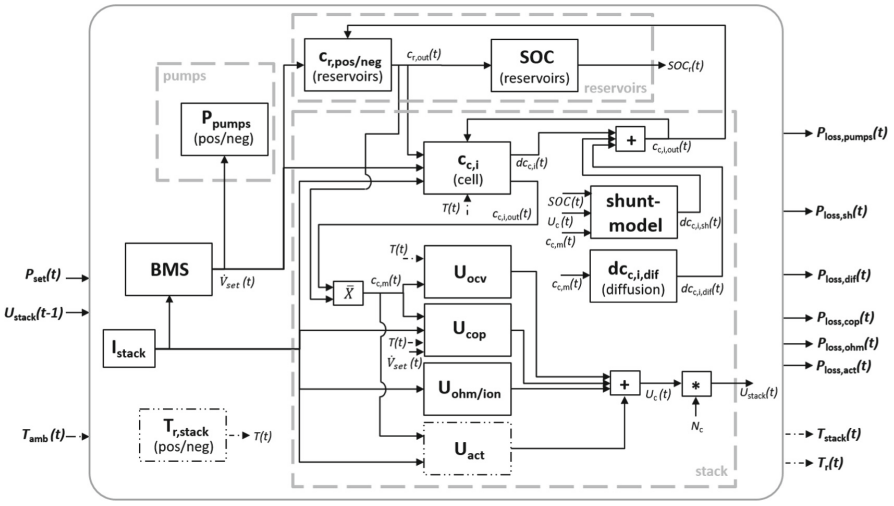

Fig. 2. Overall model of the VRFBS with the main loss mechanisms and the subcomponents.

the cell inlet and the cell outlet. The average cell concentration is a key variable to describe the stack behavior. In the individual areas, the concentrations are assumed to be largely uniformly distributed. The cell inlet concentrations of vanadium ions of a certain oxidation state always correspond to those of the reservoir. Inside the cell, the redox reaction takes place and the change in concentration can be simplified and assumed to be a linear function. The electrolyte concentration changes as a function of the current I_c and the electrolyte flow rate $\dot{V}$. This relationship can be described in simplified form by Eq. (2) [3].

$$c_{c,i,out} = c_{\mathrm{r,i}} + \frac{b \cdot N_{\mathrm{c}} \cdot I_{\mathrm{c}}}{F \cdot \dot{V}_{pos/neg}} \tag{2}$$

with $b = \begin{cases} -1 \; for \; V^{2+}/V^{5+} \\ +1 \; for \; V^{3+}/V^{4+} \end{cases}$

However, since losses due to diffusion and self-discharge occur in the cell, their influence on the concentration change must be taken into account.

3.1.2 Vanadium Diffusion

It is possible that vanadium ions diffuse through the membrane inside the cell, resulting in cross-contamination that triggers loss or self-discharge reactions in the opposite electrolyte. These processes can be quantified by the ionic flux density J_i in $mols^{-1}m^{-2}$. This is composed of the cross-sectional area A and the time derivative of the amount of substance n, as shown by Eq. (3).

$$J_i = \frac{1}{A} \cdot \frac{dn}{dt} \tag{3}$$

For this application, the ion flux density for diffusion can be described by Fick's 1st law. It indicates the amount of substance per time step that diffuses vertically through the membrane surface. It is calculated by multiplying the diffusion coefficient $k_{dif,i}^{mem}$ in $m^2 s^{-1}$ by the ratio of concentration gradient of the cell $dc_{c,i}$ and the distance x travelled according to Eq. (4) [3].

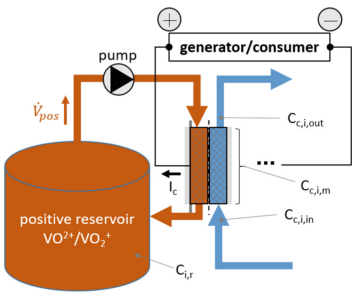

Fig. 3. Electrolyte concentrations in the VRFBS.

$$J_{dif,i} = -k_{dif,i}^{mem} \cdot \left(\frac{dc_{c,i}}{dx} \right) \tag{4}$$

The diffusion coefficient is usually determined experimentally and is already given in the literature for various membrane types [3, 4]. In the context of this work, the mean values of various literature sources for Nafion 115 are used. By multiplying the partial current density J_i with the membrane area A_{mem}, the mass transfer $\dot{n}$ can be calculated.

$$\dot{n}_i = J_i \cdot A_{mem} \tag{5}$$

If a vanadium ion diffuses through the membrane in normal mode, i.e. $0 < SOC < 1$, it reacts instantaneously and is consequently also converted directly. For example, if a V^{2+} ion from the negative half-cell (anolyte) enters the positive half-cell (catholyte), it reacts with V^{5+}. Assuming that the reaction proceeds faster than diffusion, the concentration of a vanadium ion that has diffused through the membrane into the opposite electrolyte is zero in any case. Accordingly, the following relationship holds for the concentrations in the half-cells during the operation of the system:

$$c_{c,2,pos} = c_{c,3,pos} = 0 \tag{6}$$

$$c_{c,4,neg} = c_{c,5,neg} = 0 \tag{7}$$

3.1.3 Shunt Currents

Shunt currents form a loss variable inside the stack and the piping system, where parasitic currents flow through shunt connections between the individual cells and the wiring. These can occur due to the SOC-dependent conductivity $\sigma(SOC)$ in Sm^{-1} of the electrolytes. In conjunction with the cross-sectional area A_i and the length l_i of the section through which the current flows, the resistance $R_{sh,i}$ in Ω can be calculated according to Eq. (8) [9].

$$R_{sh,i}(\mathrm{SOC}) = \frac{1}{\sigma(SOC)} \cdot \frac{l_i}{A_i} \tag{8}$$

The individual resistance of the sections can be divided into the resistances of the distribution channel R_{dist}, the meandering channel branches R_{cl}, the single cells R_c, and the reservoirs R_r. Here, rectangular cross-sectional areas are assumed for the cells and round cross-sectional areas are assumed for the channels. Since the reservoirs have no direct connection with the rest of the system, they do not need to be considered. [4]. Figure 4 shows the corresponding sections of the electrolyte circuit with the associated resistances, and Fig. 5 shows the transformation into an electrical equivalent circuit model according to the mesh analysis. For a stack with 40 cells, this results in a resistance matrix R with 156 dimensions $R \in K^{156\times156}$.

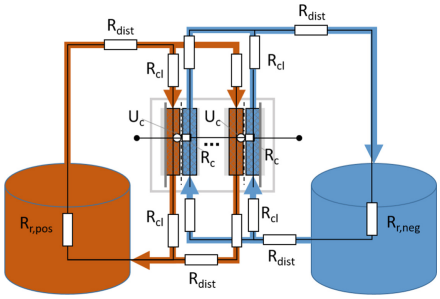

Fig. 4. Resistors to describe the electrolyte circuit corresponding to the different sections in the VRFBS.

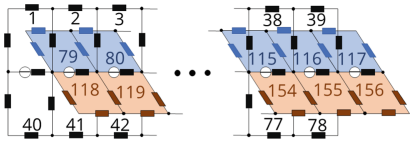

Fig. 5. Electrical equivalent circuit model for shunt currents according to mesh analysis.

Equations (9) and (10) can be used to calculate the electrolyte conductivity [4]. Here, the constant and linear terms correspond to an average value from literature sources [6] and [7].

$$\sigma_{\text{pos}} = 19.2\, Sm^{-1} + 9.0\, Sm^{-1} \cdot SOC \tag{9}$$

$$\sigma_{neg} = 29.9\, Sm^{-1} + 14.0\, Sm^{-1} \cdot SOC \tag{10}$$

In summary, values for *SOC*-dependent conductivity vary widely in the literature. Furthermore, the resistances in the single cells and in the manifold are very small compared to those of the channel branches. Therefore, they are not included in this model. Equation (11) is used for the calculation of the shunt currents. This requires the cell voltage, which is calculated from the difference between the *OCV* and the concentration overvoltages.

$$[I] = [\mathrm{R}]^{-1} \cdot [U] \tag{11}$$

3.1.4 State of Charge

The state of charge *SOC* can be determined from the ratio of the concentrations for both electrolyte circuits using Eq. (12). If the total vanadium concentration in the positive and negative circuits is the same, the results are also the same. However, if they differ, for example due to vanadium diffusion, the smaller value is taken, because a capacity loss occurs. According to this approach, the *SOC* in the reservoirs SOC_r is calculated similarly as in the single cell at the inlet SOC_{in}, at the outlet SOC_{out} and on average

SOC_m.

$$SOC = min\left(\frac{c_2}{c_2 + c_3}, \frac{c_5}{c_4 + c_5}\right) \tag{12}$$

3.2 Cell and Stack Voltage

The total cell voltage U_c can be summarized for positive currents (charging) as the sum of the individual voltage components open circuit voltage U_{OCV}, concentration overvoltage U_{cop} and the ohmic and ionic overvoltages $U_{ohm/ion}$ as shown in Eq. (13). The activation overvoltage U_{act} is neglected due to its small influence on the cell voltage and the difficult parameterization [4].

$$U_{c,ch} = U_{ocv} + U_{ohm/ion} + U_{cop} \tag{13}$$

For negative currents (discharging), the cell voltage is calculated as the difference of the open circuit voltage, the concentration overvoltage, and the absolute value of the ohmic and ionic overvoltages.

$$U_{c,dis} = U_{ocv} - \left|U_{ohm/ion}\right| - U_{cop} \tag{14}$$

The stack voltage is obtained by multiplying the cell voltage by the number N_c of cells in the stack.

$$U_{stack} = U_c \cdot N_c \tag{15}$$

3.2.1 Open Circuit Voltage

The *OCV* of the cell can be calculated using the simplified Nernst Eq. (16), which consists of a constant term, the standard potential $\tilde{E}^0$, and a variable term corresponding to the deviation from the standard conditions. For this, the gas constant R in $Jmol^{-1}K^{-1}$, the temperature T in K, the Faraday constant F in $Cmol^{-1}$ and the concentrations of the vanadium species of the reservoirs $c_{r,i}$ are required.

$$U_{OCV} = \tilde{E}^0 + \frac{R \cdot T}{F} ln\left(\frac{c_{\mathrm{r},2,\mathrm{neg}} \cdot c_{r,5,\mathrm{pos}}}{c_{r,3,\mathrm{neg}} \cdot c_{r,4,\mathrm{pos}}}\right) \tag{16}$$

According to [12], at a total vanadium concentration c_v of *1000* mol/m^3, the negative half-cell (V^{2+}/V^{3+}) has a potential of -0.255 V, and the positive half-cell (V^{4+}/V^{5+}) has a potential of *1.001* V against a standard hydrogen electrode. The potential difference is thus *1.256* V. In the real system, the standard electrode potential is slightly higher due to the Donnan potential [13]. This was tested for the presented system with the assumption that no oxidative shift takes place. This means that the initial state of the system has an average oxidation state (AOS) of the electrolyte of 3.5 ($V^{3.5+}$). The standard electrode potential theoretically corresponds to the *OCV* at a *SOC* of *0.5* (neglecting the logarithmic term). A standard potential of *1.409* V was measured at the present reference cell.

3.2.2 Ohmic and Ionic Overvoltages

The current flows from inside the cell to the current collectors, passing through various electrically conductive components. These all have electrical resistances, inducing an overvoltage and converting electrical energy into thermal energy. These ohmic overvoltages are summarized as R_{ohm}. Furthermore, there are ionic overvoltages R_{ion}, which arise due to the resistance of the electrolyte and the membrane. Both overvoltages are calculated according to Eq. (17). It is possible to calculate on the one hand with the ohmic resistance R_{ohm}, the ionic resistance R_{ion} and the cell current I_c and on the other hand with the electrode area A_e and the area-specific resistance k_{ASR} in Ωm^2.

$$U_{ohm/ion} = I_c \cdot (R_{ohm} + R_{ion}) = I_c \cdot \frac{k_{ASR}}{A_e} \tag{17}$$

3.2.3 Concentration Overvoltage

The reactions in the cell take place at the electrodes, with the reactants accumulating at their surface, resulting in an increased vanadium concentration in this region. This simultaneously leads to an overvoltage, which can be calculated with the adapted Nernst Eq. (18).

$$U_{cop} = \frac{R \cdot T}{F} ln\left(\frac{c_{c,i}}{c_{c,i,dl}}\right) \tag{18}$$

In [4], the influences of the ionic flux density J_i and the mass transfer $\dot{n}$ are also considered to obtain more accurate results in the calculation of the concentration overvoltages. In the derivation, the cell current I_c, the electrode area A_e and the mass transfer constant k_{mt} in ms^{-1} are taken into account, resulting in Eqs. (19)–(22).

$$U_{cop,dis,neg} = -\frac{R \cdot T}{F} \cdot ln\left(\frac{|I_c|}{2.38 \cdot A_e \cdot F \cdot k_{mt,neg} \cdot c_{c,2}}\right) \tag{19}$$

$$U_{cop,ch,neg} = -\frac{R \cdot T}{F} \cdot ln\left(\frac{|I_c|}{2.38 \cdot A_e \cdot F \cdot k_{mt,neg} \cdot c_{c,3}}\right) \tag{20}$$

$$U_{cop,ch,pos} = -\frac{R \cdot T}{F} \cdot ln\left(\frac{|I_c|}{2.38 \cdot A_e \cdot F \cdot k_{mt,pos} \cdot c_{c,4}}\right) \tag{21}$$

$$U_{cop,dis,pos} = -\frac{R \cdot T}{F} \cdot ln\left(\frac{|I_c|}{2.38 \cdot A_e \cdot F \cdot k_{mt,pos} \cdot c_{c,5}}\right) \tag{22}$$

wherein $\frac{|I_c|}{2.38 \cdot A_e \cdot F \cdot k_{MT-} \cdot c_{c,i}} < 1$

There are different approaches to estimate the mass transfer constant k_{mt} in the literature. According to [4], the following relations can be taken according to Eqs. (23) and (24), which use the electrolyte flow rate and the cross-sectional area of the electrode A_{cs}.

$$k_{mt,neg} = 1.608 \cdot 10^{-4} \cdot \left(\frac{\dot{V}_c}{A_{cs}}\right)^{0.4} \tag{23}$$

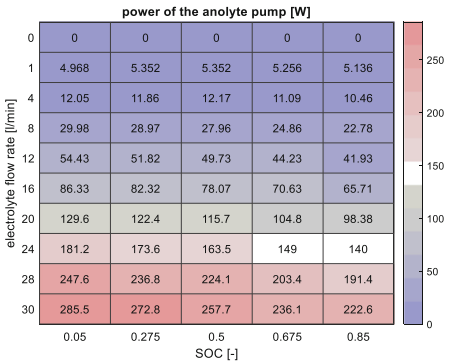

Fig. 6. Measured power consumption of the anolyte pump as a function of SOC and electrolyte flow rate.

$$k_{mt,pos} = 2.613 \cdot 10^{-4} \cdot \left(\frac{\dot{V}_c}{A_{cs}} \right)^{0.4} \tag{24}$$

3.3 Peripheral Equipment

The experimentally determined model relationship between the *SOC*, the electrolyte flow rate, and the power of the pump is described by a lookup table, for the positive and negative electrolyte, respectively. This simplifies the more complex fluid mechanical processes and provides fast results without considering numerous unknown parameters. Here, the *SOC* was measured at a working range of $SOC = [0.05; 0.85]$, respectively, for *0.05, 0.275, 0.5, 0.675* and *0.8* and the electrolyte flow rate was measured in a range of $\dot{V} = [0; 30]$ *l/min* in steps of preponderant *4* l/min. Linear interpolation is used between the results in the simulation model. The ambient temperature was 25 °C on average. The results from the tests are shown as an example for the anolyte pump in Fig. 6.

Furthermore, the energy consumption of the peripheral devices (sensors, fans, etc.) was measured for the given VRFBS and was taken into account as an average offset value in the loss analysis. A distinction can be made in a required auxiliary energy portion for normal operation and for standby operation. The results are shown in Table 1. The inverter losses are mapped via a simple efficiency curve.

3.4 Control of the Electrolyte Flow Rate

The electrolyte flow rate $\dot{V}$ in the VRFBS is specified and controlled via the battery management system. There are different control strategies for this. In the simplest case, a constant value is specified. This would not require any additional control or optimization efforts, but higher energy losses of the pumps must be expected. In addition, safety aspects such as the guarantee of a temperature range for the electrolytes or the stoichiometry are not taken into account. A common method is to calculate the minimum required flow rate in the cell $\dot{V}_{c,min}$ according to the stoichiometric ratio of the reactants.

Table 1. Power consumption of peripheral equipment.

Component	Standby	Operation
BMS	15 W	35 W
Main inverter	38 W	-
Small inverters	5 W	-
Fans	-	6.2 W
Sensors	2 W	2 W

This can be determined following Faraday's 1st law according to Eq. 25 [4]. To ensure that sufficient electrolyte flows past the electrode surface, the stoichiometric flow rate in the cell is multiplied by a safety factor $k_F > 1$ (also called Flow Factor).

$$\dot{V}_{c,min} = \begin{cases} \frac{I_c}{F \cdot (1 - SOC_r) \cdot c_v} \cdot \mathrm{k}_F(charging) \\ \frac{|I_c|}{F \cdot SOC_r \cdot c_v} \cdot \mathrm{k}_F(discharging) \end{cases} \tag{25}$$

4 Self-discharge Behavior During Standby Operation

4.1 Losses in the Stack

Since all losses in the system are investigated in an application-related context, the self-discharge in the stack and the reservoirs must also be considered when the system is at standby. For this purpose, a subdivision of the self-discharge reactions during standby into 3 states can be made analogous to *Trovo et al.* [9]: In the initial state *S0*, the $SOC > 0$, i.e. there are still V^{5+} ions in the positive half-cell and V^{2+} ions in the negative half-cell. In the transition state *S1*, it will be either $c_2 \rightarrow 0$ or $c_5 \rightarrow 0$. Due to a different rate in the reaction process and diffusion in the half-cells, this usually does not occur simultaneously, which is why a further distinction is made. State *S1a* marks the occurrence of $c_2 = 0$. In the positive half-cells, only the transferred V^{3+} ions react with V^{5+} to form two V^{4+}. State *S1b* occurs when $c_5 = 0$. Here, V^{4+} reacts with V^{2+} and H^+ in the negative half-cells to form 2 V^{3+} and H_2O. The mixing state *S2* occurs when $c_2 = 0$ and $c_5 = 0$, i.e. only diffusion of V^{3+} as well as V^{4+} takes place between the half-cells through the membrane. However, these do not react with each other, so that the concentration of V^{3+} in the positive half-cells and the concentration of V^{4+} in the negative half-cells increases until a complete mixing of V^{3+} and V^{4+} occurs (state of equimolarity). There the average oxidation state in the stack is *3.5*.

During the standby phase, only diffusion and shunt currents occur in state *S0*. In the subsequent states, the shunt currents can be neglected. Consequently, only the equations for the calculation of the cell voltage and diffusion processes are required. However, the general form of the simplified Nernst equation cannot be used to determine the *OCV*, since the numerator and denominator of the logarithm function can approach *0*. Thus, the standard potentials for the negative half-cell $\tilde{E}^{0,\mathrm{neg}}$ and positive $\tilde{E}^{0,\mathrm{pos}}$ half-cell must

Table 2. Electrolyte composition of the half-cells and their standard potentials.

State	Catholyte	Anolyte	$E^{0,pos}$	$E^{0,neg}$	E^{0}
S0	$VO^{2+}/VO_2{}^{+}$	V^{2+}/V^{3+}	1 V	-0.255 V	1,255 V
S1a	$VO^{2+}/VO_2{}^{+}$	V^{3+}/VO^{2+}	1 V	0.337 V	0.663 V
S1b	VO^{2+}/V^{3+}	V^{2+}/V^{3+}	0.337 V	-0.255 V	0.592 V
S2	VO^{2+}/V^{3+}	V^{3+}/VO^{2}	0.337 V	0.337 V	0 V

be calculated separately, using Eqs. (26) and (27) with index *'ox'* for the oxidized and index *'red'* for the reduced species [11].

$$U_{OCV,\boldsymbol{po}} = \tilde{E}^{0,\mathrm{pos}} + \frac{R \cdot T}{F} ln\left(\frac{c_{\mathrm{r,ox,pos}}}{c_{\mathrm{r,red,pos}}}\right) \tag{26}$$

$$U_{OCV,\boldsymbol{neg}} = \tilde{E}^{0,\mathrm{neg}} + \frac{R \cdot T}{F} ln\left(\frac{c_{\mathrm{r,ox,neg}}}{c_{\mathrm{r,red,neg}}}\right) \tag{27}$$

The different compositions of the electrolyte species for the individual states were summarized with the corresponding cell potentials (taken from [12]) in Table 2. For the simulation, the standard potential of the protons in the positive half-cell must be taken into account as well, which means that the potential there is about *0.154 V* higher.

For example, as can be seen in the left diagram in Fig. 7, when $SOC_{Stack} = 0.85$, a period of *11* h elapses before a significant voltage drop is observed. Such long standby times rarely occur during regular operation of the VRFBS, which means that the mixing state is usually not reached and V^{2+} and V^{5+} ions are still present in the stack. On the other hand, a large voltage drop for a $SOC = 0.15$ is already evident after *3* h. However, lower *SOC* limits of *0.05–0.1* are also common, which would lead to even shorter times for reaching a mixing state *S2*.

4.2 Losses in the Reservoirs

While losses due to vanadium diffusion and shunt currents in the cells for the de-energized condition have already been addressed in the literature [9–11], there have been no reports on self-discharge processes in the reservoirs after standby. In this context, another experimental study of this work considers the *SOC* decay in the reservoirs after different standby times. The right diagram in Fig. 7 shows the results of these experiments. Since the *SOC* in the stack drops rapidly in analogy to the stack voltage, there must also be effects on the reservoirs when the system is restarted and the discharged electrolyte is transported from the stack to the reservoirs.Therefore, four test scenarios were examined in which the entire system was placed in standby mode with a starting *SOC* of approximately *0.73* and standby durations of *24* h, *48* h, *63* h and *96* h. The system was then operated at a flow rate of *15* l/min and no load for three minutes to reach steady state. For a standby duration of *96* h, the *SOC* change in the tanks is about *12%*. Since the electrolyte volume in the stack is only about *40* l, which corresponds

to a storable energy quantity of about *800* Wh, it can be assumed that an additional self-discharge reaction takes place in the reservoirs after long standby periods.

Although both electrolytes are stored separately, i.e. there is no physical connection between them, a mass transfer can take place from the cells to the reservoirs after standby and lead to self-discharge reactions there. This must be preceded primarily by an accumulation of V^{3+} ions in the positive half-cells and V^{4+} ions in the negative half-cells. Consequently, when the system is restarted after the electrolyte has been in the mixed state, i.e. the electrolyte volume flow is greater than zero, V^{3+} ions can enter the positive reservoir and V^{4+} ions can enter the negative reservoir, leading to the following chemical reactions.

In the positive electrolyte reservoir:

$$VO_2^+ + V^{3+} \rightarrow 2VO^{2+} \tag{28}$$

In the negative electrolyte reservoir:

$$V^{2+} + VO^{2+} + 2H^+ \rightarrow 2V^{3+} + H_2O \tag{29}$$

A mathematical relationship based on chemical equilibrium and mass balance was derived for this process. The volume of the half-cells V_{hc} is assumed to be approx. *0.5* l and the volume of the reservoirs V_r approx. *420* l each. The following changes in substance quantities and concentrations take place in the negative electrolyte reservoir:

$$\Delta n_{r,2}^{neg} = -n_{c,4}^{neg} \tag{30}$$

$$\Delta n_{r,3}^{neg} = 2 \cdot n_{c,4}^{neg} + n_{c,3}^{neg} \tag{31}$$

$$\Delta c_{r,3}^{neg} = \frac{2 \cdot c_{c,4}^{neg} \cdot V_{hc} + c_{c,3}^{neg} \cdot V_{hc}}{V_r} \tag{32}$$

$$\Delta c_{r,2}^{neg} = \frac{-c_{c,4}^{neg} \cdot V_{hc}}{V_r} \tag{33}$$

Analogous relationships result for the positive electrolyte reservoirs:

$$\Delta n_{r,4}^{pos} = 2 \cdot n_{c,3}^{pos} + n_{c,4}^{pos} \tag{34}$$

$$\Delta n_{r,5}^{pos} = -n_{c,3}^{pos} \tag{35}$$

$$\Delta c_{r,4}^{pos} = \frac{2 \cdot c_{c,3}^{pos} \cdot V_{hc} + c_{c,4}^{pos} \cdot V_{hc}}{V_r} \tag{36}$$

$$\Delta c_{r,5}^{pos} = \frac{-c_{c,3}^{pos} \cdot V_{hc}}{V_r} \tag{37}$$

4.3 Verification of the Assumptions

Figure 8 shows the results of measurements and simulations of the stack voltage when the system is in standby with a *SOC* of *0.65*. In particular, when a state change is expected, a larger voltage drop occurs as described in the previous Sect. 4.1. In the present case, this would be the case at about *10* h. It is noticeable that at this point the simulation does not produce a uniform curve as seen in the measured results. Nevertheless, the values are in the same order of magnitude and show qualitative similarities for the individual sections, which makes them useful for follow-up studies.

The energy losses of the experimental investigations (s. right diagram in Fig. 7) could also be successfully reproduced with the mathematical calculation approaches from Chapter 4.2. With a starting *SOC* in the reservoirs of $SOC_{r,t0} = 0.7285$ a standby duration of *96* h has been simulated, leading to an equimolarity of the electrolytes in the stack. Therefore, after the standby, i.e., the stack is flushed with fresh electrolytes for *3* min, a new $SOC_{r,t1} = 0.6152$ could be determined in the reservoirs. This corresponds

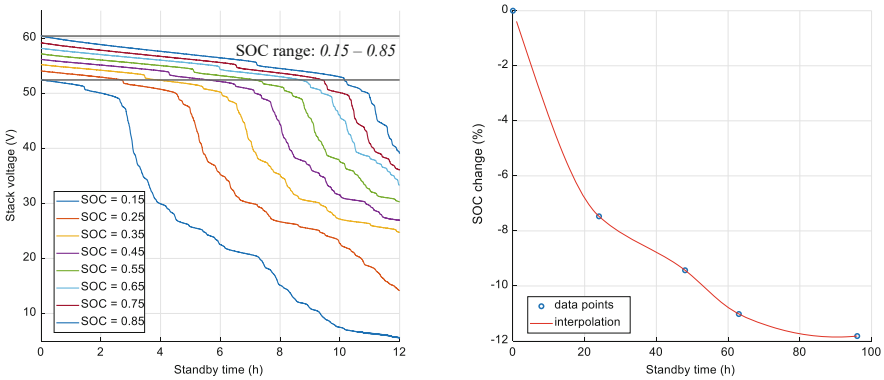

Fig. 7. Measurements of self-discharge (left) and SOC change (right) as result of voltage losses during standby.

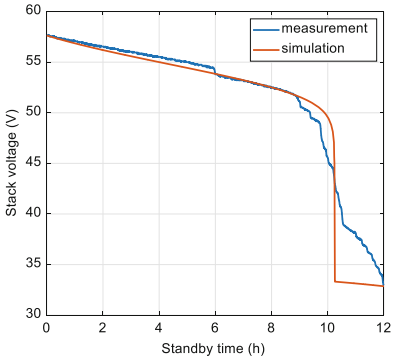

Fig. 8. Stack voltage during standby operation.

to a *SOC* change $\Delta SOC_r = -0.113$ or an energy loss of *2.04* kWh. The deviations from the measured values are of about *0.67%*, which is a good result.

5 Summary and Outlook

In this paper, results of theoretical and experimental investigations on the modeling of a commercial VRFBS were presented. Emphasis was placed on describing the various losses at the cell level (overvoltages in the stack, shunt currents and vanadium diffusion) and at the system level (consumption of peripheral components such as inverters, electrolyte pumps and battery management system). Extensive measurements were performed for qualitative studies as well as for the parameter estimation. Furthermore, this paper dealt with the experimental investigation of the self-discharge behavior during and after different standby phases. The voltage losses at different *SOC* values were modeled for the stack, and the *SOC* change after restart. The processes occurring during self-discharge were described theoretically for the voltage via a modified Nernst equation and for the concentrations via a mass balance. Simulation results and measured data show good qualitative agreement for stack voltage. The results of the investigations describing the electrolyte concentration provide a new and important insight into how critical self-discharge can be in practical VRFBS. For the reference VRFBS, a *SOC* loss of *12%* was observed after a standby period of *96* h, highlighting the importance of considering standby phases.

This problem should therefore also be taken into account and examined in greater depth in further investigations for application-related test scenarios. Furthermore, an extensive validation of the overall model is planned for the future, which will include additional experimental investigations and the use of extended parameter estimation methods. In addition, new concepts for the control of the electrolyte flow will be tested by simulation and experiment using the developed models. In particular, the increase of the system efficiency on the one hand and a gentle and lifetime-optimizing operation mode on the other hand are important. For this purpose, the overall model will be extended by an aging model for pumps and stack. In the next step, the VRFBS model will also be used and demonstrated in the context of dimensioning and energy management problems of single-use and multi-use energy storage applications. In the process, scaling of the VRFBS for larger plants will also be carried out. In addition, possibilities for using the VRFBS in hybrid energy storage configurations [11, 14] will be investigated, and potentials for increasing efficiency and lifetime will be demonstrated. New hierarchical and model-predictive energy management concepts will be based on the developed VRFBS model.

References

1. L. da Silva Lima, M. Quartier, A. Buchmayr, D. Sanjuan-Delmás, H. Laget, D. Corbisier, J. Mertens, J. Dewulf, Life cycle assessment of lithium-ion batteries and vanadium redox flow batteries-based renewable energy storage systems, Sustainable Energy Technologies and Assessments 46:101286, 2021, DOI: https://doi.org/10.1016/j.seta.2021.101286
2. SCHMID Energy Systems GmbH, Data Sheet EverFlow Compact Storage Series

3. C. Blanc, Modeling of a vanadium redox flow battery electricity storage system, École Polytechnique Fédérale de Lausanne, Dissertation, 2009, DOI: https://doi.org/10.5075/epfl-thesis-4277
4. S. König, Model-based Design and Optimization of Vanadium Redox Flow Batteries, KIT Institut für Elektroenergiesysteme und Hochspannungstechnik, Dissertation, 2017, DOI: https://doi.org/10.5445/IR/1000070670
5. A. Tang, J. Bao, M. Skyllas-Kazacos, Studies on pressure losses and flow rate optimization in vanadium redox flow battery, Journal of Power Sources, Volume 248, 2014, pp. 154-162, DOI: https://doi.org/10.1016/j.jpowsour.2013.09.071
6. F. T. Wandschneider, S. Röhm, P. Fischer, K. Pinkwart, J. Tübke, H. Nirschl, A multi-stack simulation of shunt currents in vanadium redox flow batteries, Journal of Power Sources 261, 2014, pp. 64–74, DOI: https://doi.org/10.1016/j.jpowsour.2014.03.054
7. S. Corcuera, M. Skyllas-Kazacos, State-of-charge monitoring and electrolyte rebalancing methods for the vanadium redox flow battery, European Chemical Bulletin 1, 2012, pp. 511–519
8. M. Ulaganathan, V. Aravindan, Q. Yan, S. Madhavi, M. Skyllas-Kazacos, T. M. Lim, Recent Advancements in All-Vanadium Redox Flow Batteries, Advanced Materials Interfaces 3(1), 2015, DOI: https://doi.org/10.1002/admi.201500309
9. A. Trovò, G. Marini, A. Sutto, P. Alotto, M. Giomo, F. Moro, M. Guarnieri, Standby thermal model of a vanadium redox flow battery stack with crossover and shunt-current effects, Applied Energy 240, 2019, pp. 893–906, DOI: https://doi.org/10.1016/j.apenergy.2019.02.067
10. A. Tang, J. Bao, M. Skyllas-Kazacos, Thermal modelling of battery configuration and self-discharge reactions in vanadium redox flow battery, Journal Power Sources 216, 2012, pp. 489–501, DOI: https://doi.org/10.1016/j.jpowsour.2012.06.052
11. D. You, H. Zhang, C. Sun, X. Ma, Simulation of the self-discharge process in vanadium redox flow battery. Journal of Power Sources 196, 2011, pp. 1578–1585, DOI: https://doi.org/10.1016/j.jpowsour.2010.08.036
12. A. Bard, R. Parsons, J. Jordan, Standard Potentials in Aqueous Solution, New York: CRC Press, 1985, p. 522, ISBN: 0824772911
13. K. Knehr, E.J.E.C. Kumbur, Open circuit voltage of vanadium redox flow batteries: discrepancy between models and experiments, Electrochem. Commun 13, 2011, pp. 342–345, DOI: https://doi.org/10.1016/j.elecom.2011.01.020.
14. T. Bocklisch, Hybrid energy storage approach for renewable energy applications, Journal of Energy Storage, Vol. 8, 2016. DOI: https://doi.org/10.1016/j.est.2016.01.004
15. M. Böttiger, M. Paulitschke, R. Beyer, L. Neumann, T. Bocklisch, Modular hybrid battery storage system for peak-shaving and self-consumption optimization in industrial applications, Energy Procedia, vol. 155, 2018. DOI: https://doi.org/10.1016/j.egypro.2018.11.064